

# Measurement of the $^{40}\text{Ca}(\alpha, \gamma)^{44}\text{Ti}$ reaction relevant for supernova nucleosynthesis

C. Vockenhuber,<sup>1,\*</sup> C.O. Ouellet,<sup>2</sup> L.-S. The,<sup>3</sup> L. Buchmann,<sup>1</sup> J. Caggiano,<sup>1</sup> A.A. Chen,<sup>2</sup>  
H. Crawford,<sup>1</sup> J.M. D’Auria,<sup>4</sup> B. Davids,<sup>1</sup> L. Fogarty,<sup>1</sup> D. Frekers,<sup>5</sup> A. Hussein,<sup>6</sup>  
D.A. Hutcheon,<sup>1</sup> W. Kutschera,<sup>7</sup> A.M. Laird,<sup>8</sup> R. Lewis,<sup>8</sup> E. O’Connor,<sup>1</sup> D. Ottewell,<sup>1</sup> M. Paul,<sup>9</sup>  
M.M. Pavan,<sup>1</sup> J. Pearson,<sup>2</sup> C. Ruiz,<sup>1</sup> G. Ruprecht,<sup>1</sup> M. Trinczek,<sup>1</sup> B. Wales,<sup>2</sup> and A. Wallner<sup>7</sup>

<sup>1</sup>*TRIUMF, 4004 Wesbrook Mall, Vancouver, BC, Canada V6T 2A3*

<sup>2</sup>*McMaster University, Hamilton, ON, Canada*

<sup>3</sup>*Department of Physics and Astronomy, Clemson University, Clemson, SC, USA*

<sup>4</sup>*Simon Fraser University, Burnaby, BC, Canada*

<sup>5</sup>*Institut für Kernphysik, Universität Münster, Münster, Germany*

<sup>6</sup>*University of Northern British Columbia, Prince George, BC, Canada*

<sup>7</sup>*Vienna Environmental Research Accelerator (VERA),  
Fakultät für Physik, Universität Wien, Wien, Austria*

<sup>8</sup>*University of York, York, United Kingdom*

<sup>9</sup>*Racah Institute of Physics, Hebrew University, Jerusalem, Israel*

(Dated: August 8, 2007)

The short-lived nuclide  $^{44}\text{Ti}$  is an important nuclide for the understanding of explosive nucleosynthesis. The main production reaction,  $^{40}\text{Ca}(\alpha, \gamma)^{44}\text{Ti}$ , has been studied in inverse kinematics with the recoil mass spectrometer DRAGON located at the TRIUMF-ISAC facility in Vancouver, Canada. The temperature range relevant for  $\alpha$ -rich freeze-out during a core-collapse supernova has been covered entirely with a  $^{40}\text{Ca}$  beam of 0.60 to 1.15 MeV/nucleon. All relevant quantities for the calculation of the astrophysical reaction rate have been measured directly. Due to many previously undiscovered resonances, the reaction rate derived from the energy dependent  $^{44}\text{Ti}$  yield is higher than the one based on previous prompt  $\gamma$ -ray studies commonly used in supernova models. The presented new rate results in an increased  $^{44}\text{Ti}$  production in supernovae.

PACS numbers: 25.40.Lw, 26.30.+k, 27.40.+z, 29.30.Aj, 97.10.Cv

## I. INTRODUCTION

The detection of short-lived radionuclides from supernovae provides an important tool for studying explosive nucleosynthesis [1]. The nuclide  $^{44}\text{Ti}$  is particularly well suited because it is believed to be produced in the innermost layers of core-collapse supernovae and in the normal freeze-out of Si burning layers of thermonuclear supernovae; and thus it may allow the extraction of information on the complex explosion mechanism. Additionally, its short half-life of  $58.9 \pm 0.3$  yr [2] allows a direct association with a single supernova.  $\gamma$  rays from the electron capture decay chain ( $^{44}\text{Ti} \rightarrow ^{44}\text{Sc} \rightarrow ^{44}\text{Ca}$ ) could be detected as a signature of a supernova. This was recognized long before  $\gamma$ -ray astronomy became feasible [3].

Live  $^{44}\text{Ti}$  was first observed from the  $\sim 340$  yr old Galactic supernova remnant Cassiopeia A (SNR Cas A, distance  $\sim 3.4$  kpc) with the COMPTEL telescope on board the *Compton Gamma Ray Observatory (CGRO)* detecting the characteristic 1157 keV  $\gamma$ -ray line from the subsequent decay of  $^{44}\text{Sc}$  [4]. This signal was later confirmed by the Phoswich Detection System (PDS) instrument on board *BeppoSAX*, which detected the low energy  $\gamma$  rays from the decay of  $^{44}\text{Ti}$  at 67.9 and 78.4 keV [5], and recently by the IBIS/ISGRI instrument on board

*INTEGRAL* [6]. From the measured line flux, age and distance, the mass of  $^{44}\text{Ti}$  ejected by the supernova producing Cas A could be estimated to be  $1.6_{-0.3}^{+0.6} \times 10^{-4} M_{\odot}$  [6].

For supernova SN1987A in the Large Magellanic Cloud (distance  $\sim 50$  kpc), the apparently brightest supernova in recent years, a similar amount of  $^{44}\text{Ti}$  ( $1 - 2 \times 10^{-4} M_{\odot}$  [7]) has been estimated from the light curve, which is powered in the first few years by the decay of short-lived isotopes  $^{56}\text{Ni}$  (5.9 d),  $^{56}\text{Co}$  (77.2 d) and  $^{57}\text{Co}$  (271.79 d) before the decay of  $^{44}\text{Ti}$  becomes the dominant contribution. In addition,  $^{56}\text{Ni}$  was directly observed by detecting the  $\gamma$ -ray lines from  $^{56}\text{Co}$  with the  $\gamma$ -ray spectrometer (GRS) on NASA’s *Solar Maximum Mission* satellite (*SMM*) [8]. From these observations a  $^{56}\text{Ni}$  mass of  $0.07 M_{\odot}$  was inferred [9], resulting in an abundance ratio of  $^{44}\text{Ti}/^{56}\text{Ni} \sim 2 \times 10^{-3}$ .

Other observational evidence originates from the excess of  $^{44}\text{Ca}$  relative to the other stable Ca isotopes in certain presolar grains of primitive meteorites [10]. Tiny grains (with diameters smaller than a few  $\mu\text{m}$ ) were specially selected and isotopic ratios were measured using secondary ion mass spectrometry (SIMS). Isotopic anomalies of other elements (e.g. C, N, O, Al, Si) give a clear indication of presolar origin, which means they still contain material from the time before the solar system was formed. Based on comparison with isotopic ratios predicted from supernova models, these grains are believed to be supernova condensates. The large excess of

---

\*Electronic address: christof.vockenhuber@triumf.ca

$^{44}\text{Ca}$  (up to 100 times solar) indicates a significant production from the in-situ decay of  $^{44}\text{Ti}$ . In addition, the relatively large isotopic abundance of  $^{44}\text{Ca}$  (2.086%) in the solar system can also be explained from the decay of  $^{44}\text{Ti}$  [11, 12].

Modeling supernova explosions is uncertain and complicated and only recently one begins to understand the importance of neutrinos for a successful explosion [13]. The mass of the thermal X-ray emitting gas and the amount of heavy element abundances of Cas A SNR measured by X-ray satellites are consistent with the ejecta of core-collapse supernova models. The observed abundance of  $^{44}\text{Ti}$  in Cas A is larger by a factor 2 – 10 than predicted by current 1D supernova models (e.g. [14]). The model by Limongi and Chieffi [15] gives a wide range of  $^{44}\text{Ti}$  yields depending on the kinetic energy of the explosion; however, a high  $^{44}\text{Ti}$  yield would imply a high  $^{56}\text{Ni}$  yield resulting in a bright supernova, which was not observed. The model also fails to reproduce the  $^{44}\text{Ti}/^{56}\text{Ni}$  ratio observed in SN1987A and the ratio required to explain the solar system abundance of  $^{44}\text{Ca}/^{56}\text{Fe} = 1.2 \times 10^{-3}$  (see Ref. [16] for a detailed discussion). The predictions of 1D models are complicated by the fact that the  $^{44}\text{Ti}$  yield depends critically on the location of the *mass cut*, the boundary between the material which falls back onto the neutron star or black hole and that which gets ejected and becomes available for observation. This mass cut is not well constrained. Asymmetric explosions, as supported by some observational evidence including Cas A, can result in ejection of material from deep layers, hence more  $^{44}\text{Ti}$  may be ejected while keeping the  $^{56}\text{Ni}$  yield unchanged [17, 18].

Another solution to the discrepancy could come from the half-life of  $^{44}\text{Ti}$ . Although the laboratory value is well established now after several independent measurements (see Ref. [2] and references therein), the effective half-life of  $^{44}\text{Ti}$  depends critically on the ionization state. Because the decay  $Q$ -value of  $^{44}\text{Ti}$  is 267.5 keV, it can only decay by electron capture. In the hot environment after the supernova  $^{44}\text{Ti}$  is likely highly ionized, which affects the half-life. As pointed out by Norman and Browne [19] and Motizuki and Kumagai [20], He-like  $^{44}\text{Ti}$  decays slower by a factor of 0.889, H-like by 0.444 and bare  $^{44}\text{Ti}$  is stable. This has consequences on the calculated mass of  $^{44}\text{Ti}$  from the observed line flux of Cas A and SN1987A: In the case of Cas A the calculated amount has to be lowered because of the decay correction (for H-like  $^{44}\text{Ti}$  by a factor of 2.4), whereas for SN1987A the amount has to be increased because of the lower activity which powers the light curve [20]. The main uncertainty of this correction is the unknown level of ionization of  $^{44}\text{Ti}$ .

A different aspect comes from the  $^{44}\text{Ti}$  all-sky picture. Based on the findings in Cas A, there was hope to detect more, and, in particular, previously unknown, young supernova remnants in the  $\gamma$ -ray light of  $^{44}\text{Ti}$ . A first indication of a newly discovered supernova remnant by the  $^{44}\text{Ti}$  signal in the VELA region (GRO J0852-4642) [21] was not confirmed later at the same significance level by

COMPTEL [22] and by the first set of data taken by SPI on *INTEGRAL* [23]. Thus, only one  $^{44}\text{Ti}$  source has been unambiguously identified in the sky so far. This is in stark contrast to the expected pattern taking the Galactic supernova rate of  $\simeq 3/100$  yr and contrary to the direct observation of a high yield of  $^{44}\text{Ti}$  in Cas A and SN1987A. It was thus concluded that “either core-collapse supernovae have been improbably rare in the Galaxy during the past few centuries, or  $^{44}\text{Ti}$ -producing supernovae are atypical supernovae” [24].

In order to solve that puzzle, the nuclear physics uncertainties can be reduced by improved theoretical predictions (e.g. using the statistical code NON-SMOKER [25, 26]) or by direct measurements of the rate of relevant reactions. In a large sensitivity study by The *et al.* [27] the most critical reactions have been identified. These crucially govern the  $^{44}\text{Ti}$  yield in a typical environment of the so-called  $\alpha$ -rich freeze-out from nuclear statistical equilibrium, which takes place in the last stage of a supernova explosion.  $^{44}\text{Ti}$  and  $^{56}\text{Ni}$  are produced by a series of  $\alpha$ -capture reactions on  $^{28}\text{Si}$  during the  $\alpha$ -rich freeze-out phase. In this phase a large number of  $\alpha$  particles is available because of the slowness of the triple- $\alpha$  reaction at low densities as the material cools down after the shock wave has passed. The  $^{40}\text{Ca}(\alpha, \gamma)^{44}\text{Ti}$  reaction is the dominant production reaction for  $^{44}\text{Ti}$  and has a strong influence on the final  $^{44}\text{Ti}$  yield. Its importance has also been emphasized by Hoffman *et al.* [28]. As pointed out by Rauscher *et al.* [29], reliable theoretical predictions of the rate of  $\alpha$ -capture reactions on self-conjugate ( $N = Z$ ) nuclei are difficult to make because the cross section is suppressed due to isospin effects (isospin selection rules do not allow E1  $\gamma$  transitions with  $T = 0 \rightarrow T = 0$  and M1 transitions are strongly suppressed) which are included by a somewhat arbitrary suppression factor in the statistical model. Thus, Rauscher *et al.* [29] used a semi-empirical approach to predict the  $\alpha$ -capture reaction rates on self-conjugate nuclei by comparing predictions from the NON-SMOKER code with the then-known resonance data. The NON-SMOKER rates renormalized to match the experimental data have been implemented in the supernova models [14]. On the other hand, a measurement will give a reliable reaction rate without relying on such estimates.

In this paper, we present a measurement of the  $^{40}\text{Ca}(\alpha, \gamma)^{44}\text{Ti}$  reaction rate in the entire astrophysically relevant temperature regime of  $T_9 = 1 - 2.8$  ( $T_9 = 10^9$  K) using the recoil mass spectrometer DRAGON located at the TRIUMF-ISAC facility in Vancouver, Canada.

## II. PREVIOUS MEASUREMENTS

The  $^{40}\text{Ca}(\alpha, \gamma)^{44}\text{Ti}$  reaction has been studied in the past by non-inverse prompt  $\gamma$ -ray measurements [30–34]. Most of the measurements were motivated by nuclear structure studies; only the work of Cooperman *et al.* [33] aimed to measure the reaction rate relevant for

He burning of  $^{40}\text{Ca}$  at stellar temperatures. In these measurements, a  $^{40}\text{Ca}$  target was bombarded with  $\alpha$  particles over a wide energy range corresponding to the temperature in the stellar environment. By analyzing the prompt  $\gamma$  rays from the reaction, information on the nuclear structure can be extracted and resonance strengths determined. In the energy interval of the  $\alpha$  particles  $E_\alpha = 2.75 - 4.00$  MeV (center of mass energy  $E_{\text{cm}} = 2.50 - 3.64$  MeV), corresponding to a temperature range of  $T_9 = 1.2 - 2.1$ , the resonance strengths of 12 isolated narrow resonances were measured [33]. At higher energies ( $E_\alpha = 3.79 - 5.94$  MeV,  $E_{\text{cm}} = 3.45 - 5.40$  MeV) the resonance strengths of other states were measured by Dixon *et al.* [32], including the rather strong resonance at  $E_\alpha = 4.52$  MeV ( $E_{\text{cm}} = 4.11$  MeV), which was later identified as an isospin-mixed triplet at excitation energies of  $E_x = 9.215, 9.227$  and  $9.239$  MeV [34]. The region of giant dipole resonances at  $\alpha$  energies  $E_\alpha = 6.5 - 17.5$  MeV ( $E_{\text{cm}} = 5.91 - 15.9$  MeV) were studied by Peschel *et al.* [31].

The  $Q$ -value of the  $^{40}\text{Ca}(\alpha, \gamma)^{44}\text{Ti}$  reaction was measured by comparing resonance  $\alpha$ -particle and  $\gamma$ -ray energies to a well known resonance in the  $^{15}\text{N}(\alpha, \gamma)^{19}\text{F}$  reaction with the result of  $Q = 5127.1 \pm 0.7$  keV [35].

A recent integrated cross section measurement over a larger temperature regime used the technique of off-line counting of  $^{44}\text{Ti}$  nuclei with accelerator mass spectrometry (AMS) [36–39]. In that experiment a target cell containing  $^4\text{He}$  gas was bombarded with a  $^{40}\text{Ca}$  beam and the  $^{44}\text{Ti}$  from the  $\alpha$ -capture reaction were caught by a water-cooled high purity Cu block at the end of the gas cell. The energy range covered was defined by the energy after the entrance foil and the energy loss in the He gas. The incoming  $^{40}\text{Ca}$  beam intensity was recorded as a current from the isolated and secondary electron-suppressed target chamber [36, 38]. After the irradiation, the  $^{44}\text{Ti}$  atoms were chemically extracted from the Cu catcher together with a known amount of a Ti carrier and prepared for the AMS measurement. In the AMS measurement the isotopic ratio  $^{44}\text{Ti}/\text{Ti}$  was measured, from which the number of produced  $^{44}\text{Ti}$  atoms can be calculated from the known amount of Ti carrier. Irradiations were carried out at low pressure to cover a narrow energy window around the strong resonances at  $E_x \sim 9.2$  MeV ( $E_{\text{cm}} = 4.1$  MeV) and at high pressure to cover the entire range relevant for astrophysics ( $E_x \sim 7.3 - 9.3$  MeV,  $E_{\text{cm}} \sim 2.2 - 4.17$  MeV). Whereas the result at low pressure agrees with the prompt  $\gamma$ -ray studies [37], the large-interval measurement showed a significantly larger  $^{44}\text{Ti}$  yield than the prompt  $\gamma$ -ray data would indicate [39].

The integrated resonance strength from the AMS measurement depends on the energy of contributing resonances and a range of  $\omega\gamma_{\text{int}} = 30 - 60$  eV was given [39]. This is a factor of 2.4 to 4.8 larger than the summed resonance strength ( $\sum \omega\gamma = 12.5$  eV) from the prompt  $\gamma$ -ray measurements in the same energy interval. This situation clearly demands additional measurements, given the precision of  $\sim 20\%$  needed for this important reaction.

### III. EXPERIMENTAL

#### A. $^{40}\text{Ca}$ beam

The  $^{40}\text{Ca}$  beam in our experiment was provided by the off-line ion source of the ISAC facility [40]. Due to the specifications of ISAC's radio-frequency quadrupole (RFQ) accelerator (mass to charge state ratio  $A/q \leq 30$ ) a charge state of  $2^+$  was extracted from the ion source. Special care was taken to reduce beam contamination from  $^{40}\text{Ar}$  (see Ref. [41] for details). The  $^{40}\text{Ar}$  contamination is not critical for  $^{44}\text{Ti}$  production, but high intensities of  $^{40}\text{Ar}$  can cause problems with stripper foil lifetimes and beam normalization, especially if the  $^{40}\text{Ar}/^{40}\text{Ca}$  ratio is not constant.

The  $^{40}\text{Ca}$  beam from the ion source was accelerated to 0.153 MeV/nucleon by the 35.4 MHz RFQ accelerator operating at room temperature before it was stripped to higher charge states in a thin carbon foil. Because of potential  $^{20}\text{Ne}^+$  contamination, charge state  $7^+$  was selected for further acceleration of the  $^{40}\text{Ca}$  beam in the 106 MHz variable energy drift-tube linac (DTL) to energies of  $E_b = 0.605 - 1.153$  MeV/nucleon ( $E_{\text{cm}} = 2.28 - 4.19$  MeV). In order to reduce the beam energy spread required for investigating narrow resonances and for an improved beam suppression in the spectrometer, the high- $\beta$  35.4 MHz buncher was used. By slightly debunching the beam, an energy spread of  $\Delta E/E < 0.5\%$  (FWHM) was achieved.

#### B. The recoil mass spectrometer DRAGON

We performed our measurements at the recoil mass spectrometer DRAGON (Fig. 1) which is specially designed to measure directly radiative capture reactions of astrophysical interest in inverse kinematics. In the experiment the  $^{40}\text{Ca}$  beam impinged upon a windowless gas target surrounded by a high efficiency  $\gamma$ -ray detector consisting of 30 BGO scintillator detectors closely packed to cover about 90% of the solid angle. The gas cell had a physical length of 11 cm, entrance and exit apertures of 6 and 8 mm, respectively, and was operated at pressures up to 8.5 Torr. The effective length of the gas of  $12.3 \pm 0.4$  cm was determined in an earlier work [42] by comparing energy-loss measurements with large and very small apertures. Si detectors were used to monitor beam intensity and target pressure variations continuously during the experiment by elastic scattering.

The recoil mass spectrometer consists of two stages, each with a sequence of bending magnets and electrostatic dipoles. A series of magnetic quadrupoles focuses the beam and four sextupoles correct for higher order aberrations. Beams in unselected charge states were stopped at slits after the first bending magnet (charge slits), and the one in the selected charge state at the slits after the first electrostatic dipole (mass slits). The second stage removed the beam which underwent charge

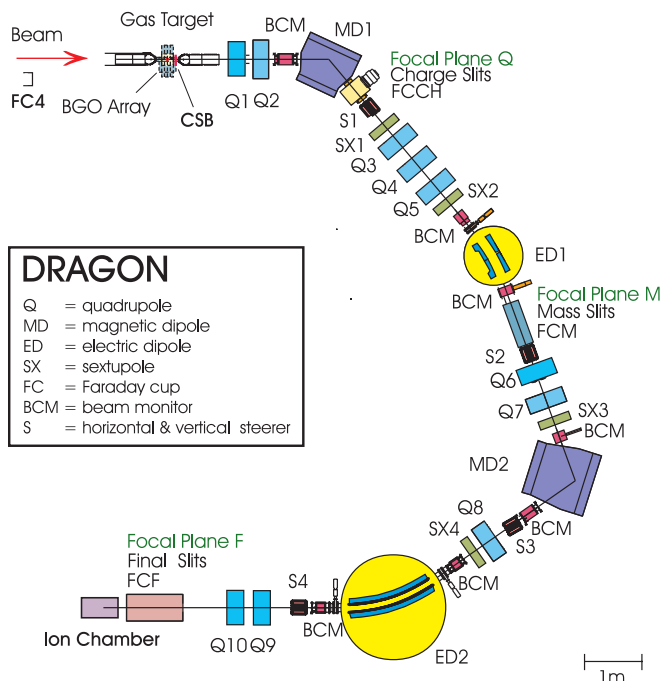


FIG. 1: (Color online) Schematic view of the DRAGON facility.

state changing or scattering processes. The total beam suppression depended on the energy and the mass/charge ( $A/q$ ) difference between recoils and beam as well as on target gas pressure and slit openings. The incoming beam quality was also crucial, especially the beam energy spread. Under certain conditions suppression factors of up to  $10^{13}$  can be obtained [43]. In our case, the beam suppression strongly depended on the selected charge state since the next lower charge state of the beam was closest in  $A/q$  (see Ref. [41] for details). As a result,  $^{40}\text{Ca}$  beam particles reaching the end detector (hereafter called ‘leaky beam’) appeared at energies lower than the  $^{44}\text{Ti}$  recoils (see Sec. IV B). The suppression factor in our experiment was in most cases around  $10^7$ . With a typical beam of 1 – 2 pA the rate at the end detector was a few hundred to a few thousand counts per second.

The  $^{44}\text{Ti}$  recoils were finally identified in an ion chamber with a segmented anode which provided two energy-loss signals and thus allowed also isobar identification. The chamber was equipped with a 1  $\mu\text{m}$  Mylar or 0.5  $\mu\text{m}$  polypropylene entrance window with a diameter of 5 cm.

Because of the high masses involved in this reaction compared to other reactions studied at DRAGON, we had to add a 100 nm silicon nitride foil a few cm downstream of the gas target [called the charge-state booster (CSB) foil] in order to reach high enough charge states so that these masses could be bent by the spectrometer [41]. Based on simulations using SRIM2003 [44] energy-loss straggling and angular scattering were calculated to be smaller than beam energy spread and the angular acceptance of the spectrometer at our energies.

Details about DRAGON separator including the data acquisition system can be found in Refs. [43, 45], and about the modifications to DRAGON for this  $^{40}\text{Ca}(\alpha, \gamma)^{44}\text{Ti}$  experiment in Ref. [41].

## IV. DATA ANALYSIS

### A. Beam normalization

The beam normalization was based on a Si detector measuring elastically scattered He atoms at an angle of  $57^\circ$ . A correlation factor independent of beam energy and target pressure between beam current and elastically scattered He atoms is given by

$$R = \frac{I}{e q} \frac{\Delta t P}{N_{\text{He}} E_b^2} \quad (1)$$

with  $N_{\text{He}}$  the number of elastically scattered He atoms within  $\Delta t$  (usually 2 min);  $I$  the beam current measured in the Faraday cup FC4 upstream of the gas target in charge state  $q$ ;  $E_b$  the  $^{40}\text{Ca}$  beam energy in keV/nucleon;  $P$  the He gas pressure in Torr and  $e = 1.602 \times 10^{-19}$  C. Dead-time losses determined from the ratio of presented to acquired triggers were taken into account. A value of  $R = 1736 \pm 105$  Torr/(keV/nucleon) $^2$  was found (Fig. 2). The uncertainty is dominated by the scatter between runs.

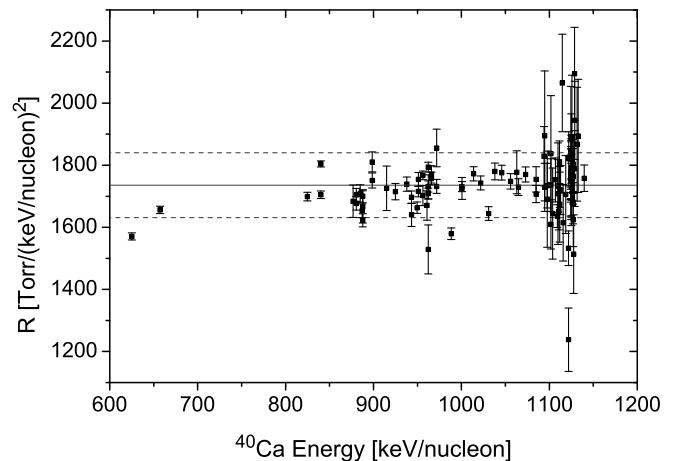


FIG. 2: Plot of  $R$ -value at various beam energies and pressures. Mean value and standard deviation are indicated as horizontal lines. Only runs where the beam was sufficiently stable in the first 2 min were selected for the calculation of the  $R$ -value.

Beam contamination was measured by running attenuated beam directly into the ion chamber, corrected for the respective charge states. Very small contamination of  $^{40}\text{Ar}$  was found:  $^{40}\text{Ar}/^{40}\text{Ca} = (1.0 \pm 0.4) \times 10^{-4}$ ,  $(4.4 \pm 0.3) \times 10^{-3}$ ,  $(6.8 \pm 0.3) \times 10^{-3}$  and  $(2.88 \pm 0.06) \times 10^{-2}$  for beam times in August 05, September 05, November 05

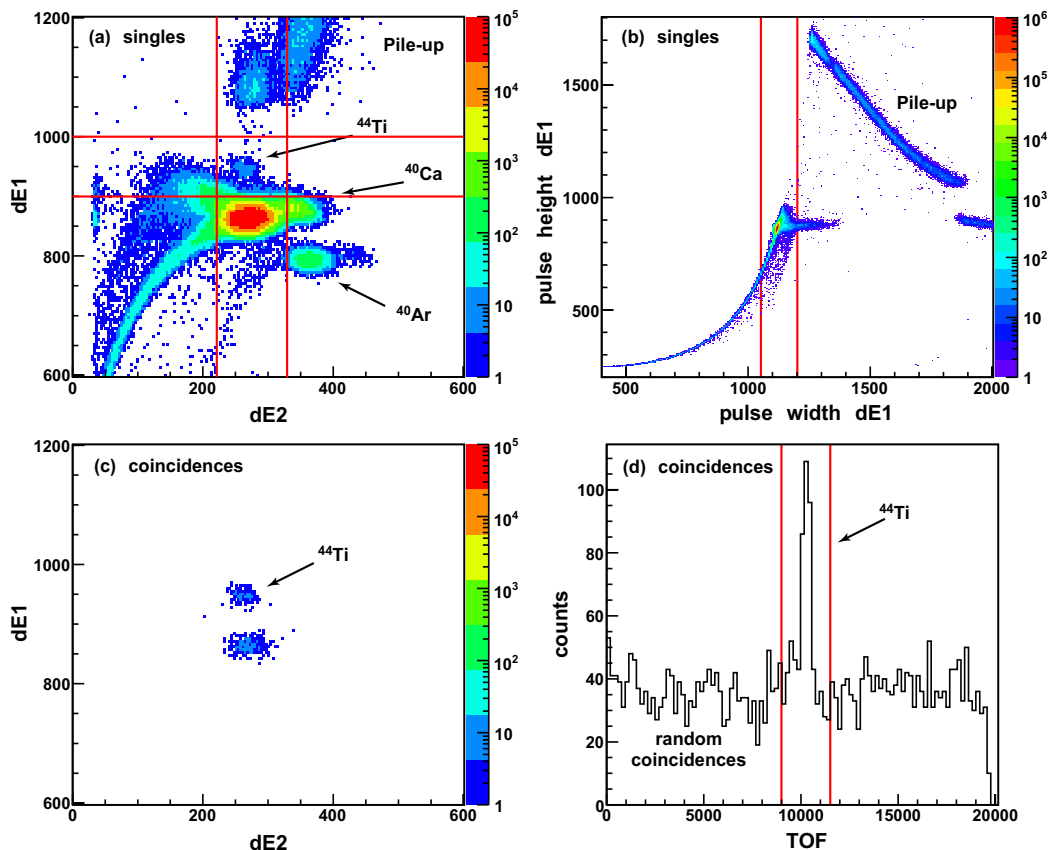


FIG. 3: (Color online) Identification of  $^{44}\text{Ti}$  recoils for a typical run at the strong resonances at  $E_x \sim 9.2$  MeV ( $^{44}\text{Ti}$  yield  $Y \sim 10^{-10}$ , total rate at the ion chamber  $\approx 3500$  s $^{-1}$ ). (a) The 2D-spectrum from the ion chamber (dE1 versus dE2) in singles shows all events reaching the end detector. The main peak is  $^{40}\text{Ca}$  leaking through the separator. A small beam contamination from  $^{40}\text{Ar}$  is also visible.  $^{44}\text{Ti}$  events are well separated at runs with high yield. (b) Pile-up is identified by plotting pulse height versus pulse width of dE1. (c) The ion chamber spectrum in coincidence with a  $\gamma$ -ray detection at the BGO array (threshold of  $\sim 2.2$  MeV,  $10$   $\mu\text{s}$  window) shows the strong reduction of  $^{40}\text{Ca}$  by more than four orders of magnitude, whereas  $^{44}\text{Ti}$  events are reduced only by the BGO efficiency (typically between 50 to 80%). (d) A time-of-flight spectrum of coincidence events allows further discrimination of  $^{44}\text{Ti}$  from leaky  $^{40}\text{Ca}$  beam with random coincidences ( $10$   $\mu\text{s}$  corresponds to 20 000 channels). Respective selection windows on the signals are shown as solid lines. All signal units are in channels.

and March 06, respectively. No indication of  $^{40}\text{K}$  contamination was found. Potential  $^{20}\text{Ne}$  contamination from the source was not present because of the mismatch of  $A/q$  with the  $^{40}\text{Ca}$  beam in charge state  $7^+$  (for details about ion sources and beam contamination see Ref. [41]).

As the  $^{40}\text{Ar}$  contamination was small, the incident  $^{40}\text{Ca}$  beam intensity was then calculated as

$$N_{40\text{Ca}} = \frac{N_{\text{He}} (1 - {}^{40}\text{Ar}/{}^{40}\text{Ca}) R E_b^2}{P}. \quad (2)$$

### B. $^{44}\text{Ti}$ identification

The  $^{44}\text{Ti}$  recoils were counted in the ion chamber at the end of the separator. As a small fraction of the incoming  $^{40}\text{Ca}$  beam was still able to reach the end detector, an identification of the ions was necessary.

The ion chamber provided two energy loss signals. This allowed a clear separation of  $^{44}\text{Ti}$  recoils from the

leaky beam particles at energies with a high yield or a high beam suppression in the separator due to the chosen charge state (Fig. 3a). A coincidence condition with a  $\gamma$ -ray detection at the BGO detectors within  $10$   $\mu\text{s}$  resulted in an efficient discrimination against events from the leaky beam (Fig. 3c). In addition, the time-of-flight information through the separator was used to further discriminate  $^{44}\text{Ti}$  against leaky  $^{40}\text{Ca}$  beam with random coincidences (Fig. 3d). Pile-up at high counting rates was identified by recording pulse height as well as the pulse width of the first energy-loss signal (Fig. 3b).

A final discrimination was reached by the recorded energies of the  $\gamma$  rays. Since the sum of all emitted  $\gamma$  rays cannot exceed the energy of the excitation level, that information was used to further identify true  $^{44}\text{Ti}$  events.

On all conditions wide cuts were chosen in order not to lose any good events. The multiple selection steps allowed measurements of a  $^{44}\text{Ti}/{}^{40}\text{Ca}$  ratio in the  $10^{-14}$  range.

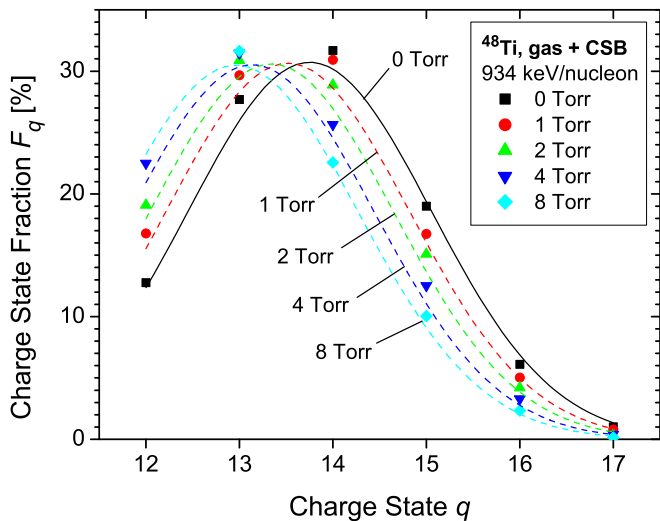


FIG. 4: (Color online) Charge state distribution of Ti at 934 keV/nucleon after the charge state booster foil and various gas target pressures measured with stable  $^{48}\text{Ti}$ . Small leakage of gas downstream of the foil shifts the distribution towards lower charge states. The solid curve represents the prediction from the Sayer formula [46]; the dashed curves are calculated using the modified Sayer formula (see text).

### C. Ti charge state distributions

The charge state fraction of  $^{44}\text{Ti}$  recoils was determined by measuring charge state distributions of stable  $^{48}\text{Ti}$ . Four  $^{48}\text{Ti}$  beam energies (537, 702, 826 and 934 keV/nucleon) were chosen to cover the measured energy range of  $^{44}\text{Ti}$  recoils. Gas target pressures were varied from 0 to 4 Torr, with and without the charge state booster foil.

The charge state distribution of Ti after a solid stripper could be well reproduced by the semi-empirical formula of Sayer [46] (see Fig. 4). However, during running conditions with several Torr of He in the gas target, a small fraction of the gas leaked downstream of the foil resulting in a small shift of the charge state distribution towards lower charge states. The shift depended on the pressure in the gas target. To account for this effect we shifted the mean charge state from the Sayer formula depending on an empirical correlation of the gas pressure and the energy, while keeping the rest of the calculation the same. This approximation reproduced the measured charge state fractions reasonably well (Fig. 4).

The charge state distribution with gas only was also investigated, which was particularly important for the measurements at lower  $^{40}\text{Ca}$  energies ( $E_b \lesssim 850$  keV/nucleon) which were taken without the charge state booster foil. Because of the bending requirements of the first magnetic dipole (MD1) only three charge states with a measurable current could be investigated (Fig. 5). The equilibrium charge state distribution was reached within 1 – 2 Torr corresponding to an energy

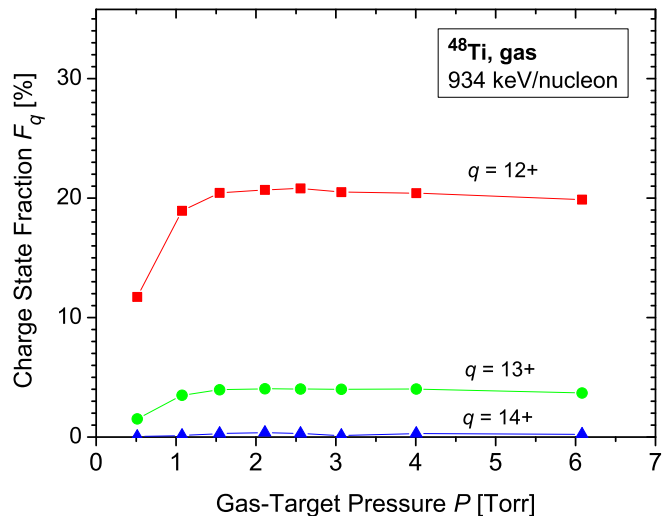


FIG. 5: (Color online) Charge state distribution of Ti at 934 keV/nucleon without the charge state booster foil as a function of gas target pressures measured with stable  $^{48}\text{Ti}$ . Equilibrium is reached within 1 – 2 Torr.

loss of 2.5 – 5 keV/nucleon. Thus, yield measurements without the charge state booster foil were taken with a slightly larger overlap in energy.

We assigned an uncertainty of 5% ( $1\sigma$ ) to the charge state fraction in the resonance strength calculation.

### D. BGO efficiency

The efficiency of the BGO  $\gamma$ -ray detector array was estimated by comparing ion chamber spectra in singles and coincidence as well as by a Monte Carlo simulation of DRAGON using GEANT3 [47]. The full geometry of the DRAGON setup, i.e. the BGO detector array and the recoil spectrometer, was simulated and resulting spectra were convoluted with the response function of the detectors. Since the maximum possible cone angle of our reaction at the covered energies was small ( $< 5.5$  mrad) compared to the nominal angular acceptance of the spectrometer, the transmission was close to 100% for recoils in the selected charge state. Thus, only the results of the  $\gamma$ -ray detection were used in our simulation of the efficiency. In order to keep the statistical uncertainty small, 20 000 reactions were simulated for each scenario.

Detection of  $\gamma$  rays from decay of a  $^{44}\text{Ti}$  excited state required that at least one detector of the BGO array registered a signal above the hardware trigger threshold. Thus, the BGO efficiency depended both on the threshold setting and on the  $\gamma$ -ray decay scheme of each resonance. The threshold was approximated in the simulation by fitting half of a Gaussian function to the low-energy edge of the measured background spectrum. The hardware trigger threshold was set to different values at different stages in the experiment and varied between  $1.1 \pm 0.17$

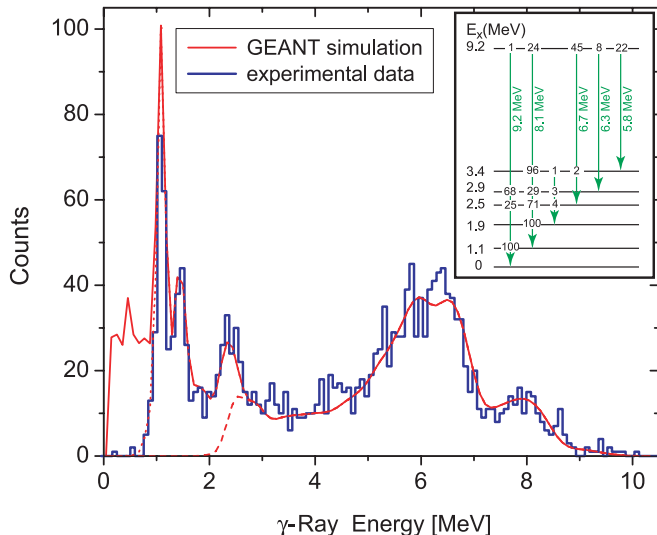


FIG. 6: (Color online) The  $\gamma$ -ray spectrum (all BGO detectors added) at the three strong resonances ( $E_x \sim 9.2$  MeV) of the most energetic  $\gamma$  ray in coincidence with  $^{44}\text{Ti}$  detection (histogram). The spectrum is well reproduced by the GEANT3 simulation (solid curve) with the trigger threshold set to  $1.1 \pm 0.17$  MeV (dotted line). The influence of a higher threshold at  $2.8 \pm 0.3$  MeV as set at an earlier stage of the experiment is also shown (dashed line). The inset shows a level diagram with the  $\gamma$ -ray branching ratios [48] of the dominant middle resonance (70% contribution).

and  $2.8 \pm 0.3$  MeV.

In particular, the three strong resonances at  $E_x \sim 9.2$  MeV were simulated with the branching ratios taken from Ref. [48]. Figure 6 shows a measured spectrum of the most energetic  $\gamma$  ray in each event which is well reproduced by the GEANT3 simulation and the setting of the threshold. Despite different branching in the deexcitation of the three resonances (here referred to as ‘lower’, ‘middle’ and ‘upper’ resonance) only small differences in the efficiency were observed. For example, at the highest threshold ( $2.8 \pm 0.3$  MeV) the simulation gave 58.3%, 57.7% and 60.6% for the ‘lower’, ‘middle’ and ‘upper’ resonance, respectively. In addition, two extreme cases were simulated as well: One with a pure ground-state transition, i.e. one  $\gamma$  ray with the full energy of the level, resulting in an efficiency of 59.6%; the other with a hypothetical cascade with several 1 MeV- $\gamma$  rays, leading to only 6.6%. In that case the energy of the most energetic  $\gamma$  ray is below the threshold, and thus only pulse pile-up events would be registered.

Due to the energy resolution of the BGO detectors [ $\sim 7\%$  (FWHM) at 6.13 MeV] and the high multiplicity of the  $\gamma$  rays (see e.g. the deexcitation of middle resonance shown in the inset in Fig. 6), a discrimination between similar branchings is not possible. However, a  $\gamma$ - $\gamma$  analysis of recorded spectra allowed us to observe a dominant ground-state transition. A cascade with only sub-threshold  $\gamma$  rays would be hard to see in the  $\gamma$ -ray

spectra, if the most energetic  $\gamma$  ray is below the threshold. However, there is no evidence of such cases for this reaction at the excitation energies of this experiment: the lowest observed coincidence/singles ratio was around 0.5; of the resonances measured previously with Ge detectors, the decay of a given level produced at least a  $\gamma$  ray of 4.8 MeV or higher.

From our simulations we can conclude that as long as the energy of one  $\gamma$  ray is above the trigger threshold, the efficiency depends mainly on the level of that threshold, while it is rather insensitive to the branching ratios. The influence of the excitation energy is also small: the efficiency is reduced from 57.7% to 55.9% when the excitation level is reduced from 9.227 MeV (middle resonance) to 7.634 MeV (i.e. the last energy where we could clearly see  $^{44}\text{Ti}$  events) assuming the same branching as for the middle resonance.

Thus, we use the efficiency for one given trigger threshold from observed coincidence/singles ratio. For the stronger resonances,  $^{44}\text{Ti}$  ions could be identified cleanly in the ion chamber spectra, without requiring coincident  $\gamma$ -ray detection. This ratio can be directly compared with the predicted BGO efficiencies from the GEANT3 simulations. We find efficiencies for the four trigger threshold settings of  $52 \pm 7\%$ ,  $50 \pm 4\%$ ,  $58 \pm 4\%$  and  $80 \pm 5\%$ , respectively, which is in good agreement with the predictions from the GEANT3 simulations.

We used a 10% systematic uncertainty, determined from comparisons of simulations with source measurements [47], in the calculated efficiencies.

### E. Yield and resonance strength

The measured yield, which is the number of recoiling  $^{44}\text{Ti}$  nuclei per incoming  $^{40}\text{Ca}$  projectile for a particular energy interval, is calculated from

$$Y = \frac{N_{^{44}\text{Ti}}}{N_{^{40}\text{Ca}} F_q \epsilon}, \quad (3)$$

with  $F_q$  the charge state fraction and  $\epsilon$  the detection efficiency of the  $^{44}\text{Ti}$  recoils; the latter includes the transmission through the spectrometer and the efficiency of the end detector, both close to 100%. If coincidence with the  $\gamma$  rays is used then  $\epsilon$  includes the efficiency of the BGO detector array,  $\epsilon_{\text{BGO}}$ .

The resonance strength is defined by:

$$\omega\gamma = \frac{2J_R + 1}{(2J_t + 1)(2J_p + 1)} \frac{\Gamma_\alpha \Gamma_\gamma}{\Gamma} \quad (4)$$

with  $J_R$ ,  $J_t$  and  $J_p$  the spins of the resonance, target and ground state of projectile, respectively;  $\Gamma_\alpha$ ,  $\Gamma_\gamma$  the partial  $\alpha$  and  $\gamma$  widths of the resonance, and  $\Gamma = \Gamma_\alpha + \Gamma_\gamma$ . From the measured yield  $Y$ ,  $\omega\gamma$  can be calculated based on the thick target yield formalism:

$$\omega\gamma = \frac{2}{\lambda^2} \frac{m_t}{m_p + m_t} \left( \frac{dE}{dx} \right) Y \quad (5)$$

with  $\lambda$  the de Broglie wavelength of the center of mass system;  $m_p$  and  $m_t$  the masses of projectile and target; and  $dE/dx$  the stopping power of the projectile in the target in the laboratory system.

If more than one resonance is covered in the energy interval  $\Delta E$ , the measured yield  $Y$  contains contributions from all resonances, and thus equation 5 gives the integrated resonance strength  $\omega\gamma_{\text{int}}$ .

### F. $^{40}\text{Ca}$ beam energy and stopping power in He

The  $^{40}\text{Ca}$  beam energy was measured using the calibrated magnetic field of the first magnetic dipole MD1. Since MD1 is not strong enough to bend the beam in the incoming charge state ( $7^+$ ), the beam energy was measured at several pressures and then linearly extrapolated to zero pressure. The stopping power was derived from the slope of the linear fit. Together with the gas target thickness the stopping power could be directly determined, which is necessary to convert the measured yield into a resonance strength.

Figure 7 shows the measured data over the energies covered in this experiment compared to predictions from SRIM2003 [49]. No experimental data are available for  $^{40}\text{Ca}$  in He [50]. Our measurements suggest that the stopping power is 10% lower, thus we used the SRIM2003 stopping power multiplied by a factor of 0.9 throughout our calculations.

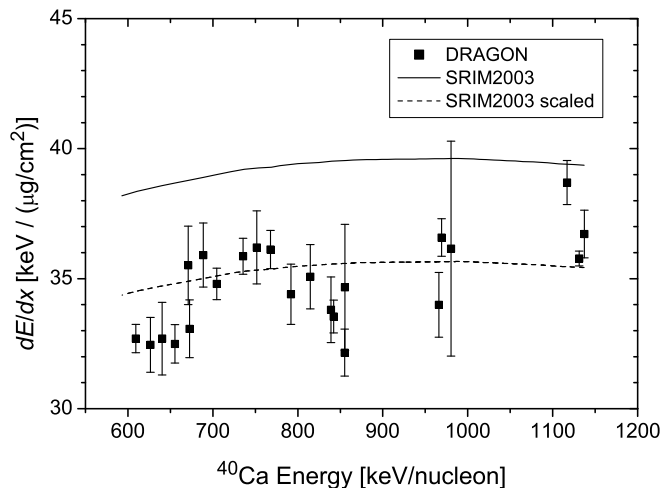


FIG. 7: The stopping power for  $^{40}\text{Ca}$  in He measured at DRAGON (data points) and predicted by SRIM2003 (solid line). The data are reproduced best by the SRIM2003 calculations scaled by a factor of 0.9 (dashed line).

### G. Uncertainties

The statistical uncertainties are dominated by the counting statistics of the  $^{44}\text{Ti}$  events with only a mi-

nor contribution from the elastically scattered He atoms used in the beam normalization. The systematic uncertainties are summarized in Table I. Uncertainties from beam contaminations are negligible. All systematic errors are added in quadrature. The laboratory energy range covered in each run was extended by 5 keV/nucleon (2.5 keV/nucleon at either side) in order to account for the systematic uncertainties in the determination of the beam energy. This uncertainty is propagated to the de Broglie wavelength  $\lambda$  calculation in equation 5.

TABLE I: Compilation of systematic uncertainties ( $1\sigma$ ).

Source of uncertainty	Uncertainty
beam normalization, $R$	6%
BGO efficiency, $\epsilon_{\text{BGO}}$	10%
charge state fraction, $F_q$	5%
stopping power, $dE/dx$	5%
energy uncertainty	5 keV/nucleon

## V. RESULTS AND DISCUSSION

### A. Excitation function

From the incident  $^{40}\text{Ca}$  beam energy  $E_b$ , the energy loss in the gas target  $\Delta E$ , and the measured yield  $Y$ , an excitation function can be plotted (Fig. 8). In our experiment we covered a  $^{40}\text{Ca}$  beam energy range from 1153 down to 605 keV/nucleon with more than 100 energy steps. Most of the data points were taken at a target pressure of 4 Torr (corresponding to an energy interval of  $\Delta E \sim 10$  keV/nucleon). Below  $E_b \approx 850$  keV/nucleon data were taken at 8 Torr (and without the CSB foil) with extended  $\Delta E$  overlap in order to cover the entire range with the condition of charge state equilibrium of the recoils (see Sec. IV C). In Table II the points selected for the calculation of the reaction rate are listed.

For comparison we calculated the yield from the resonances with known resonance strength (taken from Ref. [48]) using the scaled stopping power from SRIM2003 (see Sec. IV F) and plotted them as vertical lines in Fig. 8. The uncertainties of the excitation energies ( $\pm 2$  to  $\pm 6$  keV depending on the level; the lowest two resonances at  $^{40}\text{Ca}$  energies of 689 keV/nucleon and 808 keV/nucleon have an uncertainty of  $\pm 20$  keV) and the respective uncertainties in the resonance strength are not shown by these lines.

For the strong resonances at  $E_x \sim 9.2$  MeV, a yield of  $Y = (9.8 \pm 1.3) \times 10^{-11}$  was measured in the  $^{40}\text{Ca}$  energy interval 1123 – 1136 keV/nucleon, which corresponds to an integrated resonance strength of  $\omega\gamma_{\text{int}} = 7.6 \pm 1.0$  eV. This is in good agreement with the summed resonance strength of  $\sum \omega\gamma = 8.3 \pm 0.4$  eV of the resonances at  $E_x = 9.215, 9.227$  and  $9.239$  MeV, the thin target measurement of Ref. [39] with  $\omega\gamma_{\text{int}} = 8.8 \pm 3.0$  eV and our preliminary

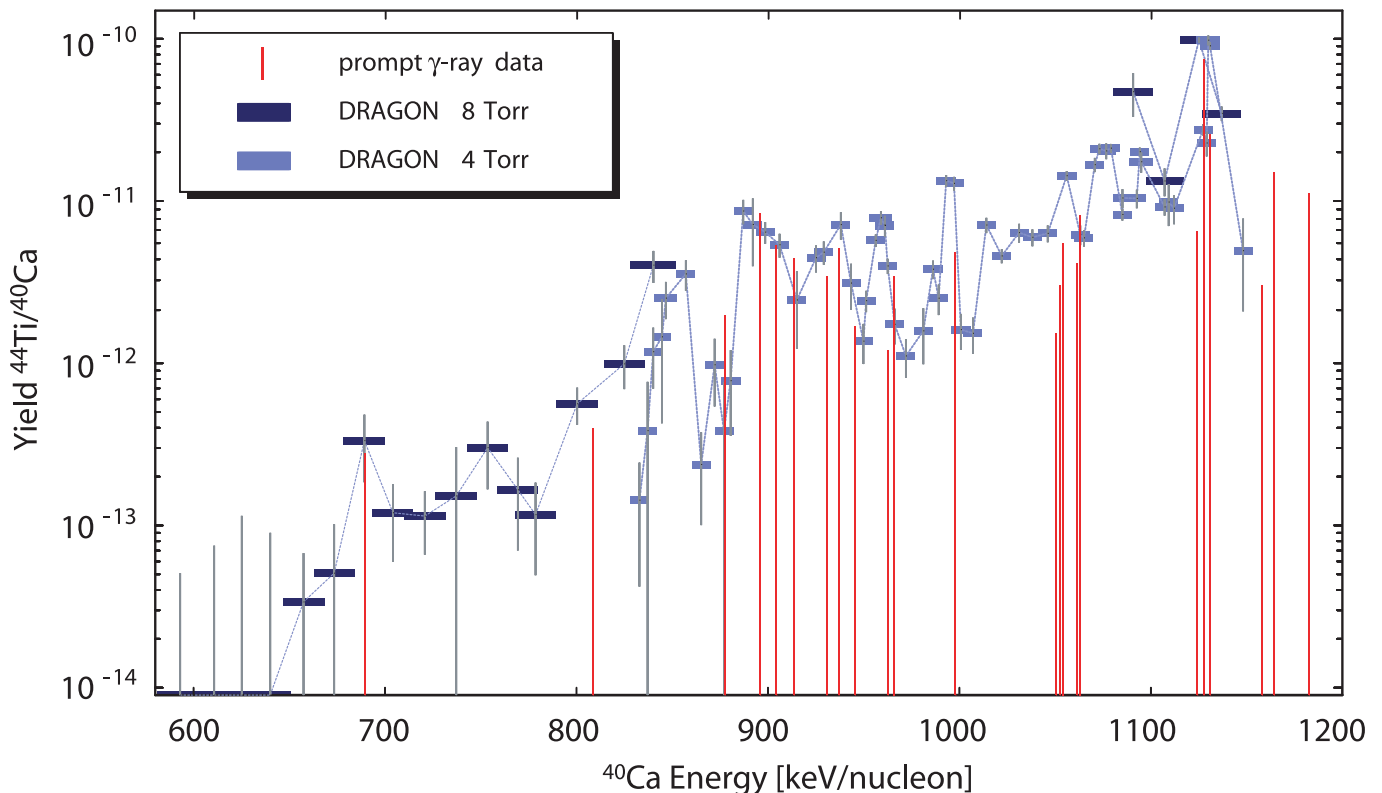


FIG. 8: (Color online) Excitation function of the  $^{40}\text{Ca}(\alpha,\gamma)^{44}\text{Ti}$  reaction measured at DRAGON. Data sets at 4 Torr and 8 Torr are indicated in different shades, and the connecting lines are only to guide the eye. The yield at each measurement point depends on how many narrow resonances are hit, and thus overlapping bars at different pressures agree with each other only if the same resonances are hit in both cases. At the four lowest energies we observed only upper limits. For comparison, vertical lines indicate known resonance strengths from prompt  $\gamma$ -ray studies.

value of  $\omega\gamma_{\text{int}} = 7.7 \pm 0.7$  eV [41]. The yield at this energy was repeatedly measured during several beam times at various charge states and gas target pressures and gives confidence in corrections for charge state fraction and BGO efficiency, and in the insensitivity to characteristics of the  $^{40}\text{Ca}$  beam.

For other energies we find discrepancies. Comparing the  $^{40}\text{Ca}$  energy interval 875 – 998 keV/nucleon covered also by Cooperman *et al.* [33], we find an integrated yield higher by a factor of 2. In general, at the energies where a resonance strength was published, we see a similar yield. However, from the gaps between the resonances identified by the prompt  $\gamma$ -ray studies, we can conclude that information about resonances was missing in these measurements.

### B. Astrophysical reaction rate

The astrophysical reaction rate in units of  $\text{cm}^3 \text{s}^{-1} \text{mole}^{-1}$  is calculated as follows [51]:

$$N_A \langle \sigma \nu \rangle = 1.540 \times 10^{11} / (\mu T_9)^{3/2} \sum_{i=1}^N (\omega\gamma)_i e^{-11.605 E_i / T_9} \quad (6)$$

where  $N_A$  is Avogadro's number;  $\langle \sigma \nu \rangle$  the thermally averaged reaction rate per particle pair;  $\mu$  is the reduced mass in atomic mass units and  $T_9$  the temperature in  $10^9$  K. For all selected  $N$  energy intervals, the integrated resonance strength  $\omega\gamma_i$  at the center of the covered energy range in the center of mass,  $E_i$ , is used; both in units of MeV. Uncertainties from the resonance strength itself and from the unknown positions of the resonances within that energy range are taken into account with the code RATEERRORS [52]. Contributions from resonances at energies beyond our highest beam energy (taken from Ref. [48]) were included in the calculation of the reaction rate. It should be noted that only six resonances with measured resonance strengths are known for energies  $E_x \gtrsim 9.3$  MeV which is rather incomplete. From the many resonances seen in the measurement of Ref. [32], only a few were selected for their complete analysis. However, as discussed later (Sec. V D), the reaction rate corresponding to these high energies is not critical for  $^{44}\text{Ti}$  production during the  $\alpha$ -rich freeze-out.

The resulting reaction rate is listed in Table III, and shown in Fig. 9 together with the reaction rate deduced from prompt  $\gamma$ -ray studies (hereafter called ‘Prompt Gamma’) and the one given by the integral measurement by Nassar *et al.* [39] (hereafter called ‘Nassar2006’).

TABLE II:  $^{40}\text{Ca}$  energies, yields and resonance strengths of the  $^{40}\text{Ca}(\alpha, \gamma)^{44}\text{Ti}$  reaction measured at DRAGON. Only data used to calculate the reaction rate are listed.  $E_b$  is the beam energy and  $\Delta E$  the energy loss in the gas target (without the 5 keV/nucleon energy uncertainty).

$E_b$ [keV/nucleon]	$\Delta E$	$Y$ [ $10^{-11}$ ]	$\omega\gamma$ [eV]
1153.0	9.7	$0.494 \pm 0.285$	$0.389 \pm 0.231$
1147.0	14.6	$3.078 \pm 0.582$	$2.407 \pm 0.562$
1135.0	11.0	$9.810 \pm 0.322$	$7.602 \pm 1.070$
1117.0	19.7	$1.330 \pm 0.261$	$1.011 \pm 0.242$
1099.0	9.6	$1.962 \pm 0.110$	$1.476 \pm 0.218$
1090.0	9.7	$0.870 \pm 0.062$	$0.649 \pm 0.100$
1078.0	3.8	$2.098 \pm 0.091$	$1.553 \pm 0.223$
1068.0	7.9	$0.604 \pm 0.054$	$0.442 \pm 0.072$
1061.0	10.0	$1.433 \pm 0.097$	$1.042 \pm 0.159$
1051.0	9.8	$0.632 \pm 0.076$	$0.455 \pm 0.083$
1043.0	9.7	$0.597 \pm 0.072$	$0.427 \pm 0.078$
1036.0	9.7	$0.639 \pm 0.085$	$0.454 \pm 0.087$
1027.0	9.8	$0.459 \pm 0.046$	$0.323 \pm 0.055$
1019.0	9.8	$0.711 \pm 0.077$	$0.497 \pm 0.087$
1005.8	3.6	$0.157 \pm 0.028$	$0.109 \pm 0.024$
998.1	5.8	$1.313 \pm 0.083$	$0.901 \pm 0.136$
991.2	6.9	$0.321 \pm 0.036$	$0.219 \pm 0.039$
986.0	9.7	$0.158 \pm 0.060$	$0.107 \pm 0.043$
977.0	9.9	$0.111 \pm 0.030$	$0.074 \pm 0.022$
971.0	9.7	$0.174 \pm 0.043$	$0.116 \pm 0.033$
965.0	8.9	$0.760 \pm 0.062$	$0.503 \pm 0.080$
956.2	9.8	$0.243 \pm 0.037$	$0.160 \pm 0.032$
948.3	9.8	$0.312 \pm 0.099$	$0.203 \pm 0.070$
943.0	9.9	$0.716 \pm 0.138$	$0.463 \pm 0.109$
930.0	5.7	$0.467 \pm 0.058$	$0.298 \pm 0.055$
920.0	9.8	$0.245 \pm 0.123$	$0.155 \pm 0.080$
911.0	9.9	$0.538 \pm 0.091$	$0.336 \pm 0.073$
903.5	9.9	$0.643 \pm 0.098$	$0.398 \pm 0.082$
897.0	9.8	$0.717 \pm 0.320$	$0.441 \pm 0.206$
892.0	9.8	$0.868 \pm 0.149$	$0.531 \pm 0.116$
885.5	10.0	$0.078 \pm 0.042$	$0.047 \pm 0.027$
877.0	9.7	$0.098 \pm 0.044$	$0.059 \pm 0.028$
870.0	9.7	$0.024 \pm 0.014$	$0.014 \pm 0.008$
862.0	9.8	$0.355 \pm 0.076$	$0.210 \pm 0.053$
852.0	23.6	$0.402 \pm 0.090$	$0.233 \pm 0.061$
835.6	21.3	$0.099 \pm 0.030$	$0.056 \pm 0.019$
811.1	21.5	$0.056 \pm 0.015$	$0.031 \pm 0.009$
789.3	21.3	$0.012 \pm 0.007$	$0.006 \pm 0.004$
780.0	21.2	$0.017 \pm 0.010$	$0.009 \pm 0.005$
764.2	21.3	$0.030 \pm 0.013$	$0.016 \pm 0.007$
748.0	21.6	$0.015 \pm 0.015$	$0.008 \pm 0.008$
731.5	21.4	$0.011 \pm 0.005$	$0.006 \pm 0.002$
714.7	21.1	$0.012 \pm 0.006$	$0.006 \pm 0.003$
700.1	21.7	$0.033 \pm 0.015$	$0.016 \pm 0.007$
684.1	21.3	$0.005 \pm 0.005$	$0.002 \pm 0.002$
668.2	21.5	$0.003 \pm 0.003$	$0.001 \pm 0.002$
651.0	21.9	$< 0.008^a$	
635.8	21.2	$< 0.011^a$	
622.0	22.5	$< 0.007^a$	
604.8	23.6	$< 0.004^a$	

<sup>a</sup>Not used for calculation of the reaction rate.

TABLE III: The  $^{40}\text{Ca}(\alpha, \gamma)^{44}\text{Ti}$  reaction rate measured at DRAGON (LL –  $1\sigma$  lower limit, rate – best rate, UL –  $1\sigma$  upper limit).

$T_9$	$N_A \langle \sigma v \rangle$ [ $\text{cm}^3 \text{s}^{-1} \text{mole}^{-1}$ ]		
	LL	rate	UL
1	$1.17 \times 10^{-10}$	$1.78 \times 10^{-10}$	$2.70 \times 10^{-10}$
1.1	$1.56 \times 10^{-09}$	$2.27 \times 10^{-09}$	$3.29 \times 10^{-09}$
1.2	$1.37 \times 10^{-08}$	$1.91 \times 10^{-08}$	$2.65 \times 10^{-08}$
1.3	$8.84 \times 10^{-08}$	$1.18 \times 10^{-07}$	$1.58 \times 10^{-07}$
1.4	$4.48 \times 10^{-07}$	$5.77 \times 10^{-07}$	$7.44 \times 10^{-07}$
1.5	$1.87 \times 10^{-06}$	$2.33 \times 10^{-06}$	$2.91 \times 10^{-06}$
1.6	$6.65 \times 10^{-06}$	$8.07 \times 10^{-06}$	$9.80 \times 10^{-06}$
1.7	$2.07 \times 10^{-05}$	$2.46 \times 10^{-05}$	$2.91 \times 10^{-05}$
1.8	$5.77 \times 10^{-05}$	$6.71 \times 10^{-05}$	$7.79 \times 10^{-05}$
1.9	$1.46 \times 10^{-04}$	$1.67 \times 10^{-04}$	$1.90 \times 10^{-04}$
2	$3.40 \times 10^{-04}$	$3.83 \times 10^{-04}$	$4.31 \times 10^{-04}$
2.1	$7.37 \times 10^{-04}$	$8.20 \times 10^{-04}$	$9.13 \times 10^{-04}$
2.2	$1.50 \times 10^{-03}$	$1.65 \times 10^{-03}$	$1.82 \times 10^{-03}$
2.3	$2.87 \times 10^{-03}$	$3.14 \times 10^{-03}$	$3.44 \times 10^{-03}$
2.4	$5.22 \times 10^{-03}$	$5.69 \times 10^{-03}$	$6.20 \times 10^{-03}$
2.5	$9.09 \times 10^{-03}$	$9.86 \times 10^{-03}$	$1.07 \times 10^{-02}$
2.6	$1.52 \times 10^{-02}$	$1.64 \times 10^{-02}$	$1.78 \times 10^{-02}$
2.7	$2.46 \times 10^{-02}$	$2.65 \times 10^{-02}$	$2.85 \times 10^{-02}$
2.8	$3.85 \times 10^{-02}$	$4.13 \times 10^{-02}$	$4.44 \times 10^{-02}$
2.9	$5.85 \times 10^{-02}$	$6.27 \times 10^{-02}$	$6.71 \times 10^{-02}$
3	$8.66 \times 10^{-02}$	$9.25 \times 10^{-02}$	$9.88 \times 10^{-02}$
3.1	$1.25 \times 10^{-01}$	$1.33 \times 10^{-01}$	$1.42 \times 10^{-01}$
3.2	$1.77 \times 10^{-01}$	$1.88 \times 10^{-01}$	$2.00 \times 10^{-01}$
3.3	$2.45 \times 10^{-01}$	$2.60 \times 10^{-01}$	$2.76 \times 10^{-01}$
3.4	$3.33 \times 10^{-01}$	$3.53 \times 10^{-01}$	$3.74 \times 10^{-01}$
3.5	$4.45 \times 10^{-01}$	$4.71 \times 10^{-01}$	$4.99 \times 10^{-01}$
3.6	$5.85 \times 10^{-01}$	$6.19 \times 10^{-01}$	$6.55 \times 10^{-01}$
3.7	$7.59 \times 10^{-01}$	$8.01 \times 10^{-01}$	$8.47 \times 10^{-01}$
3.8	$9.71 \times 10^{-01}$	$1.02 \times 10^{+00}$	$1.08 \times 10^{+00}$
3.9	$1.23 \times 10^{+00}$	$1.29 \times 10^{+00}$	$1.36 \times 10^{+00}$
4	$1.53 \times 10^{+00}$	$1.61 \times 10^{+00}$	$1.70 \times 10^{+00}$
4.1	$1.89 \times 10^{+00}$	$1.99 \times 10^{+00}$	$2.10 \times 10^{+00}$
4.2	$2.31 \times 10^{+00}$	$2.43 \times 10^{+00}$	$2.56 \times 10^{+00}$
4.3	$2.80 \times 10^{+00}$	$2.94 \times 10^{+00}$	$3.10 \times 10^{+00}$
4.4	$3.36 \times 10^{+00}$	$3.53 \times 10^{+00}$	$3.72 \times 10^{+00}$
4.5	$4.00 \times 10^{+00}$	$4.20 \times 10^{+00}$	$4.42 \times 10^{+00}$
4.6	$4.73 \times 10^{+00}$	$4.96 \times 10^{+00}$	$5.22 \times 10^{+00}$
4.7	$5.55 \times 10^{+00}$	$5.82 \times 10^{+00}$	$6.12 \times 10^{+00}$
4.8	$6.47 \times 10^{+00}$	$6.78 \times 10^{+00}$	$7.12 \times 10^{+00}$
4.9	$7.49 \times 10^{+00}$	$7.85 \times 10^{+00}$	$8.24 \times 10^{+00}$
5	$8.62 \times 10^{+00}$	$9.04 \times 10^{+00}$	$9.47 \times 10^{+00}$
5.1	$9.87 \times 10^{+00}$	$1.03 \times 10^{+01}$	$1.08 \times 10^{+01}$
5.2	$1.12 \times 10^{+01}$	$1.18 \times 10^{+01}$	$1.23 \times 10^{+01}$
5.3	$1.27 \times 10^{+01}$	$1.33 \times 10^{+01}$	$1.39 \times 10^{+01}$
5.4	$1.43 \times 10^{+01}$	$1.50 \times 10^{+01}$	$1.57 \times 10^{+01}$
5.5	$1.61 \times 10^{+01}$	$1.69 \times 10^{+01}$	$1.76 \times 10^{+01}$

### C. Comparison to statistical models

Reaction rates for the  $^{40}\text{Ca}(\alpha, \gamma)^{44}\text{Ti}$  reaction are available from several statistical model codes based on the Hauser-Feshbach approach [53]. Here we compare our reaction rate with the ones from the recent libraries,

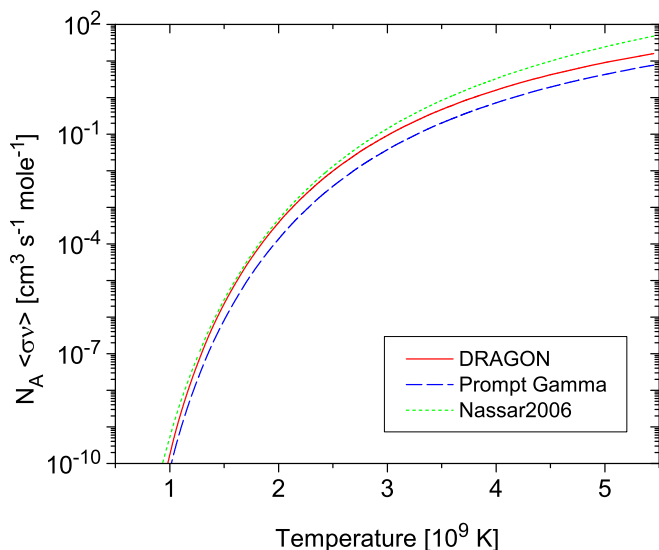


FIG. 9: (Color online) The astrophysical reaction rate of  $^{40}\text{Ca}(\alpha,\gamma)^{44}\text{Ti}$  calculated from the measurement at DRAGON (solid line) as a function of temperature. For comparison, other reaction rates based on measurements from the prompt  $\gamma$ -ray studies (dashed line) and from the integral measurement by Nassar *et al.* [39] (dotted line) are shown.

i.e. REACLIB with the NON-SMOKER rates [25][60] and BRUSLIB based on the MOST statistical model [54]. The Hauser-Feshbach approach gives reliable predictions if the level density in the compound nucleus is high enough which is usually the case for nuclei heavier than  $A \approx 40$  and close to the valley of stability.

In addition, we include the reaction rates derived from the semi-empirical model by Rauscher *et al.* [29] in which the NON-SMOKER rate was compared with available data of resonances in order to predict  $\alpha$ -capture reaction rates on self-conjugate ( $N = Z$ ) nuclei more reliably. This reaction rate (hereafter called ‘Rauscher Empirical’) is almost identical to the Prompt Gamma rate and is used in the supernova model in Ref. [14].

Figure 10 shows the comparison of the theoretical and experimental reaction rates relative to the Prompt Gamma rate. For the DRAGON rate and for the Prompt Gamma rate the uncertainty range is also shown. The Nassar2006 rate is a scaled BRUSLIB rate, where the isospin suppression factor was increased from  $f_{\text{iso}} = 5$  to  $f_{\text{iso}} = 8$  to match the average cross section derived from their integral measurement and the BRUSLIB model. It should be noted, that the stopping power of  $^{40}\text{Ca}$  in He gas from SRIM2003 was used to calculate the average cross section [39]. From our measurement of the stopping power (see Sec. IV F), the cross section has to be lowered by 10%, and therefore the Nassar2006 rate should be also lower.

The ratios of theoretical rates over the measured ones all show a steep increase towards lower temperatures below  $T_9 \approx 1$ , because there are no measured resonances at lower energies which dominate the reaction rate in that

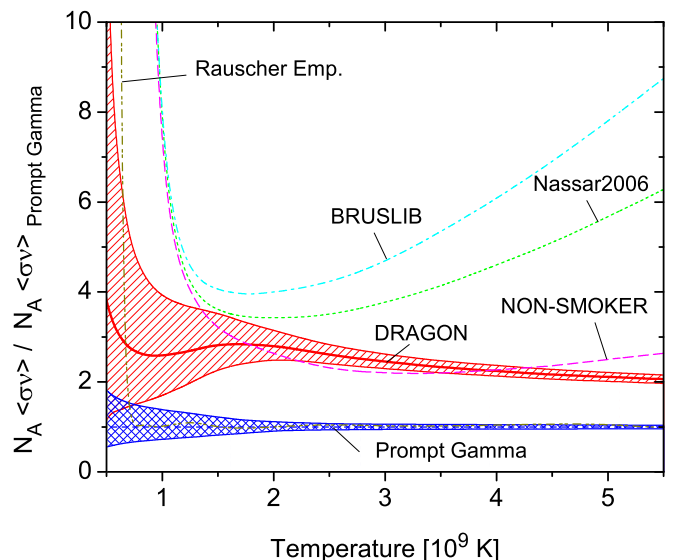


FIG. 10: (Color online) Comparison of the  $^{40}\text{Ca}(\alpha,\gamma)^{44}\text{Ti}$  reaction rates relative to the rate calculated from the prompt  $\gamma$ -ray studies. The hatched area for the DRAGON and Prompt Gamma rates represents experimental uncertainties.

region. The same is true, although to a smaller extent, for the higher temperatures above  $T_9 \approx 3$ , because of missing experimental information. In the energy range relevant for  $\alpha$ -rich freeze-out conditions ( $T_9 \approx 1 - 2.8$ ), the DRAGON rate is about a factor of three higher than the Prompt Gamma rate. The BRUSLIB rate is higher by a factor of  $> 4$ ; the Nassar2006 rate about a factor of 3.5 to 4.

The DRAGON rate is best reproduced by the NON-SMOKER rate, although there are differences in the shape of the curve. This is surprising since it was argued in Ref. [29] that the level density in  $^{44}\text{Ti}$  is not high enough for a reliable prediction for the statistical model. That was the reason that the semi-empirical rate was believed to be more reliable. A low level density is also supported by  $\alpha$ -transfer reactions [55, 56], at least at excitation energies below  $\approx 8.5$  MeV. Similarly, elastic  $\alpha$ -scattering in this region which shows almost resolved compound nucleus resonances indicates that the level density is low [57, 58]. However, our excitation function clearly shows a higher level density than known at the time when the semi-empirical comparison was done [29].

#### D. Astrophysical implications

The influence of different available reaction rates for  $^{40}\text{Ca}(\alpha,\gamma)^{44}\text{Ti}$  on the  $^{44}\text{Ti}$  production in the  $\alpha$ -rich freeze-out was investigated with the model described in Ref. [27], in which the adiabatic expansion of pure  $^{28}\text{Si}$  matter at an initial peak temperature of  $T_9 = 5.5$  and peak density of  $\rho = 10^7$  g cm $^{-3}$  is simulated. Contrary to the initial sensitivity study with the reaction rates

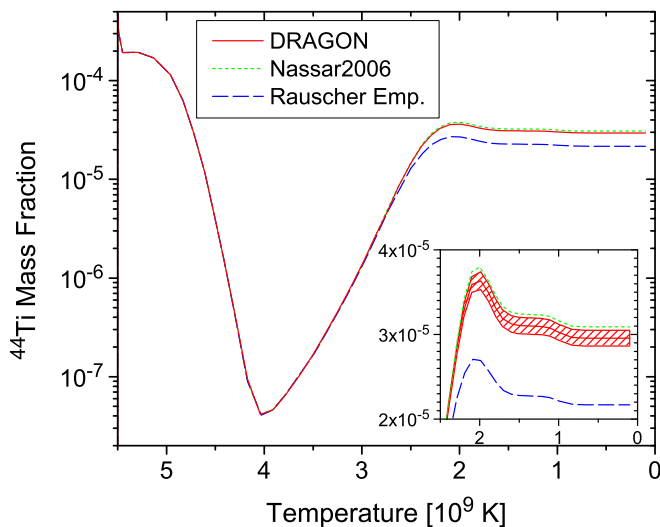


FIG. 11: (Color online)  $^{44}\text{Ti}$  mass fraction as a function of temperature in the  $\alpha$ -rich freeze-out (peak temperature  $T_9 = 5.5$ , peak density  $\rho = 10^7 \text{ g cm}^3$ , neutron excess  $\eta = 0$ ) calculated for the reaction rates of DRAGON (solid line, hatched area), of Nassar *et al.* [39] (dotted line) and of the semi-empirical model by Rauscher *et al.* [29] (dashed line). The inset shows the  $^{44}\text{Ti}$  mass fraction at low temperatures in more detail with a linear scale.

taken from the SMOKER code [59] the improved rates from NON-SMOKER [25] were used.

Figure 11 is similar to Fig. 2 of Ref. [27] and shows the evolution of the mass fraction of  $^{44}\text{Ti}$  in the adiabatic expansion starting at  $T_9 = 5.5$  with equal total number of neutrons and protons ( $\eta = 0$ ). The general behavior of the mass fraction can be explained as follows: At the high initial temperatures a large quasi-equilibrium (QSE) cluster of nuclei is formed from reactions with light particles from the break up of  $^{28}\text{Si}$ . Within this cluster, the reaction rates are the same as for the inverse reaction. The fraction of  $^{44}\text{Ti}$  drops with the falling temperature because the QSE cluster moves to higher masses. At around  $T_9 = 4$   $^{44}\text{Ti}$  breaks out of the QSE cluster and its abundance starts to grow again because it is formed by a series of  $\alpha$ -capture reactions starting with the triple- $\alpha$  reaction. Compared to the initial study with the SMOKER rates [27]  $^{44}\text{Ti}$  breaks out of the QSE cluster at a lower temperature ( $T_9 = 4$  *versus*  $T_9 = 4.3$ ) which results in  $^{44}\text{Ti}$  yield lower by a factor of 10.

The final mass fraction of  $^{44}\text{Ti}$ ,  $X(^{44}\text{Ti})$ , was calculated for the available reaction rates as discussed in Sec. VB and VC and the results are summarized in Table IV. Compared to the Rauscher Empirical rate which is used in the supernova model in Ref. [14] the DRAGON rate shows an increase of about 40%. The uncertainty of the DRAGON rate is represented by the lower limit rate (LL) and upper limit rate (UL). The range corresponds to a small variation of  $\pm 3\%$  ( $1\sigma$ ). Note that our upper limit of the final  $^{44}\text{Ti}$  mass fraction is slightly lower than the  $^{44}\text{Ti}$  mass fraction inferred from the Nassar2006 rec-

TABLE IV:  $^{44}\text{Ti}$  mass fraction  $X(^{44}\text{Ti})$  calculated with available  $^{40}\text{Ca}(\alpha, \gamma)^{44}\text{Ti}$  reaction rates (LL – lower limit, UL – upper limit).

rate	$X(^{44}\text{Ti}) [\times 10^{-5}]$	LL $[\times 10^{-5}]$	UL $[\times 10^{-5}]$
DRAGON	2.957	2.864	3.049
PromptGamma	2.160	2.094	2.240
Nassar2006	3.089		
Rauscher Emp.	2.169		
NON-SMOKER	2.749		
BRUSLIB	3.216		

ommended rate. However, as mentioned in Sec. VB the Nassar2006 rate has to be lowered due to the lower value of the stopping power determined experimentally in this work and thus their result will lie within the range from the DRAGON measurement.

Prior to the experiment the sensitivity of  $X(^{44}\text{Ti})$  on the  $^{40}\text{Ca}(\alpha, \gamma)^{44}\text{Ti}$  reaction rate at different temperatures was investigated. Table V shows the result with respect to the standard calculation when the standard rate is multiplied by a factor of 10 or divided by 100, respectively, at various temperature intervals. As expected, no change in the final  $^{44}\text{Ti}$  yield is observed in the high temperature regime ( $T_9 > 4.3$ ) because of the equilibrium condition. Between  $T_9 = 4.3$  and  $T_9 = 2.8$ , only a small dependence on the reaction rate can be seen. Changes of the reaction rate below  $T_9 = 2.8$  result in a large variation of the final  $^{44}\text{Ti}$  yield. A similar value can be found if the rate is changed in the entire temperature range. From the results of the original study [27], the  $^{44}\text{Ti}$  production dependence on the  $^{40}\text{Ca}(\alpha, \gamma)^{44}\text{Ti}$  reaction rate is not sensitive to  $\eta$ . Thus, the results from the temperature sensitivity study at  $\eta = 0$  is also valid for conditions with a neutron excess  $\eta > 0$ .

TABLE V: Sensitivity of the  $^{44}\text{Ti}$  mass fraction  $X(^{44}\text{Ti})$  on rate changes at different temperatures.

$T_9$ range	$X(^{44}\text{Ti}) [\times 10^{-5}]$	
	rate $\times 10$	rate $\times 0.01$
Standard <sup>a</sup>	2.0685	
$T_9 > 4.3$	2.0685	2.0684
$4.3 > T_9 > 2.8$	2.0683	2.0726
$T_9 < 1.0$	2.0685	2.0685
$T_9 < 2.8$	3.7922	0.1626
$T_9 < 5.5$	3.7921	0.2819

<sup>a</sup>The rates were taken from Ref. [25].

## VI. SUMMARY

The  $^{40}\text{Ca}(\alpha, \gamma)^{44}\text{Ti}$  reaction responsible for the production of  $^{44}\text{Ti}$  in supernovae has been measured in the energy interval  $E_{\text{cm}} = 2.11 - 4.19 \text{ MeV}$  at the recoil mass

spectrometer DRAGON in inverse kinematics by detecting  $^{44}\text{Ti}$  recoils and prompt  $\gamma$  rays. As a temperature sensitivity study shows, the entire energy range relevant in the  $\alpha$ -rich freeze-out phase has been covered. Compared to previous studies in normal kinematics with a  $^4\text{He}$  beam impinging on a  $^{40}\text{Ca}$  target and measuring prompt  $\gamma$  rays, an increased  $^{44}\text{Ti}$  yield was observed – mainly resulting from yield between resonances known from previous studies. This suggests that the level density in  $^{44}\text{Ti}$  is higher than previously thought. The fact that the statistical model code NON-SMOKER represents our reaction rate in the measured temperature range reasonably well supports this suggestion. The direct measurement of all relevant quantities for the calculation of the astrophysical reaction rate improves the accuracy of our result. With our reaction rate the final  $^{44}\text{Ti}$  mass fraction in a simulation of the  $\alpha$ -rich freeze-out is about

40% higher compared to the semi-empirical rate from Ref. [29] commonly used in supernova models. The uncertainty of our measurement results in a small uncertainty of  $\pm 3\%$  in the final calculated mass fraction.

### Acknowledgments

Special thanks goes to Keerthi Jayamanna, Marco Marchetto, Bob Laxdal and the entire ISAC operations crew for delivering  $^{40}\text{Ca}$  beam to DRAGON and for the many energy changes. We also want to thank Peter Machule and Don Dale especially for the assistance with the DRAGON electrostatic dipoles. Financial support from the Natural Science and Engineering Research Council of Canada is gratefully acknowledged.

- 
- [1] R. Diehl, N. Prantzos, and P. von Ballmoos, Nucl. Phys. **A 777**, 70 (2006).
- [2] I. Ahmad, J. P. Greene, E. F. Moore, S. Ghelberg, A. Ofan, M. Paul, and W. Kutschera, Phys. Rev. C. **74**, 065803 (2006).
- [3] D. D. Clayton, S. A. Colgate, and G. J. Fishman, Astrophys. J. **155**, 75 (1969).
- [4] A. F. Iyudin, R. Diehl, H. Bloemen, W. Hermsen, G. G. Lichti, D. Morris, J. Ryan, V. Schoenfelder, H. Steinle, M. Varendorff, et al., Astron. Astrophys. **284**, L1 (1994).
- [5] J. Vink, J. M. Laming, J. S. Kaastra, J. A. M. Bleeker, H. Bloemen, and U. Oberlack, Astrophys. J. **560**, L79 (2001).
- [6] M. Renaud, J. Vink, A. Decourchelle, F. Lebrun, P. R. den Hartog, R. Terrier, C. Couvreur, J. Knödseder, P. Martin, N. Prantzos, et al., Astrophys. J. **647**, L41 (2006).
- [7] Y. Motizuki and S. Kumagai, in *Tours Symposium on Nuclear Physics V*, edited by M. Arnould, M. Lewitowicz, G. Münzenberg, H. Akimune, M. Ohta, H. Utsunomiya, T. Wada, and T. Yamagata (2004), vol. 704 of *American Institute of Physics Conference Series*, pp. 369–374.
- [8] S. M. Matz, G. H. Share, M. D. Leising, E. L. Chupp, and W. T. Vestrand, Nature **331**, 416 (1988).
- [9] W. D. Arnett, J. N. Bahcall, R. P. Kirshner, and S. E. Woosley, Ann. Rev. Astr. Astrophys. **27**, 629 (1989).
- [10] L. R. Nittler, S. Amari, E. Zinner, S. E. Woosley, and R. S. Lewis, Astrophys. J. **462**, L31 (1996).
- [11] D. Bodansky, D. D. Clayton, and W. A. Fowler, Astrophys. J. Suppl. **16**, 299 (1968).
- [12] S. E. Woosley, W. D. Arnett, and D. D. Clayton, Astrophys. J. Suppl. **26**, 231 (1973).
- [13] H.-T. Janka, K. Langanke, A. Marek, G. Martínez-Pinedo, and B. Müller, Phys. Rep. **442**, 38 (2007).
- [14] T. Rauscher, A. Heger, R. D. Hoffman, and S. E. Woosley, Astrophys. J. **576**, 323 (2002).
- [15] M. Limongi and A. Chieffi, Astrophys. J. **592**, 404 (2003).
- [16] N. Prantzos, in *ESA SP-552: 5th INTEGRAL Workshop on the INTEGRAL Universe*, edited by V. Schoenfelder, G. Lichti, and C. Winkler (2004), pp. 15–.
- [17] K. Maeda and K. Nomoto, Astrophys. J. **598**, 1163 (2003).
- [18] K. Nomoto, N. Tominaga, H. Umeda, C. Kobayashi, and K. Maeda, Nucl. Phys. **A 777**, 424 (2006).
- [19] E. B. Norman and E. Browne, in *Origin of Elements in the Solar System, Implications of Post-1957 Observations*, edited by O. Manuel (2000), pp. 211–216.
- [20] Y. Motizuki and S. Kumagai, New Astr. Rev. **48**, 69 (2004).
- [21] A. F. Iyudin, V. Schönfelder, K. Bennett, H. Bloemen, R. Diehl, W. Hermsen, G. G. Lichti, R. D. van der Meulen, J. Ryan, and C. Winkler, Nature **396**, 142 (1998).
- [22] V. Schönfelder, H. Bloemen, W. Collmar, R. Diehl, W. Hermsen, J. Knödseder, G. G. Lichti, S. Plüschke, J. Ryan, A. Strong, et al., in *American Institute of Physics Conference Series*, edited by M. L. McConnell and J. M. Ryan (2000), vol. 510 of *American Institute of Physics Conference Series*, pp. 54–59.
- [23] A. von Kienlin, D. Attié, S. Schanne, S. Cordier, R. Diehl, A. F. Iyudin, G. G. Lichti, J.-P. Roques, V. Schönfelder, and A. Strong, in *ESA SP-552: 5th INTEGRAL Workshop on the INTEGRAL Universe*, edited by V. Schoenfelder, G. Lichti, and C. Winkler (2004), pp. 87–.
- [24] L.-S. The, D. D. Clayton, R. Diehl, D. H. Hartmann, A. F. Iyudin, M. D. Leising, B. S. Meyer, Y. Motizuki, and V. Schönfelder, Astron. Astrophys. **450**, 1037 (2006).
- [25] T. Rauscher and F.-K. Thielemann, Atomic Data and Nuclear Data Tables **75**, 1 (2000).
- [26] T. Rauscher and F.-K. Thielemann, Atomic Data and Nuclear Data Tables **79**, 47 (2001).
- [27] L.-S. The, D. D. Clayton, L. Jin, and M. S. Meyer, Astrophys. J. **504**, 500 (1998).
- [28] R. D. Hoffman, S. E. Woosley, T. A. Weaver, T. Rauscher, and F.-K. Thielemann, Astrophys. J. **521**, 735 (1999).
- [29] T. Rauscher, F.-K. Thielemann, J. Goerres, and M. Wiescher, Nucl. Phys. **A 675**, 695 (2000).
- [30] J. J. Simpson, W. R. Dixon, and R. S. Storey, Phys. Rev. **C 4**, 443 (1971).
- [31] R. E. Peschel, J. M. Long, H. D. Shay, and D. A. Brom-

- ley, Nucl. Phys. **A 232**, 269 (1974).
- [32] W. R. Dixon, R. S. Storey, and J. J. Simpson, Phys. Rev. **C 15**, 1896 (1977).
- [33] E. L. Cooperman, M. H. Shapiro, and H. Winkler, Nucl. Phys. **A 284**, 163 (1977).
- [34] W. R. Dixon, R. S. Storey, and J. J. Simpson, Can. J. Phys. **58**, 1360 (1980).
- [35] W. R. Dixon, R. S. Storey, and A. F. Bielajew, Nucl. Phys. **A 378**, 273 (1982).
- [36] S. K. Hui, M. Paul, D. Berkovits, E. Boaretto, S. Gehlberg, M. Hass, A. Hershkowitz, and E. Navon, Nucl. Instr. Meth. **B 172**, 642 (2000).
- [37] M. Paul, C. Feldstein, I. Ahmad, D. Berkovits, C. Bordenau, J. Caggiano, S. Gehlberg, J. Goerres, J. Greene, M. Hass, et al., Nucl. Phys. **A 718**, 239c (2003).
- [38] H. Nassar, M. Paul, S. Ghelberg, A. Ofan, N. Trubnikov, Y. Ben-Dov, M. Hass, and B. S. N. Singh, Nucl. Phys. **A 758**, 411 (2005).
- [39] H. Nassar, M. Paul, I. Ahmad, Y. Ben-Dov, J. Caggiano, S. Ghelberg, S. Goriely, J. P. Greene, M. Hass, A. Heger, et al., Phys. Rev. Lett. **96**, 041102 (2006).
- [40] R. E. Laxdal, Int. Workshop on production of radioactive ion beams (PRORIB 2001), Pui, India, 200, URL: [www.triumf.ca/download/lax/prorib2000/prorib2001\\_paper/prorib2000\\_3.pdf](http://www.triumf.ca/download/lax/prorib2000/prorib2001_paper/prorib2000_3.pdf) (2001).
- [41] C. Vockenhuber, C. O. Ouellet, L. Buchmann, J. Caggiano, A. A. Chen, J. M. D'Auria, D. Frekers, A. Hussein, D. A. Hutcheon, W. Kutschera, et al., Nucl. Instr. Meth. **B 259**, 688 (2007).
- [42] U. Greife, S. Bishop, L. Buchmann, M. L. Chatterjee, A. A. Chen, J. M. D'Auria, S. Engel, D. Gigliotti, D. Hunter, D. A. Hutcheon, et al., Nucl. Instr. Meth. **B 217**, 1 (2004).
- [43] S. Engel, D. A. Hutcheon, S. Bishop, L. Buchmann, J. Caggiano, M. L. Chatterjee, A. A. Chen, J. M. D'Auria, D. Gigliotti, U. Greife, et al., Nucl. Instr. Meth. **A 553**, 491 (2005).
- [44] J. F. Ziegler, Nucl. Instr. Meth. **B 219**, 1027 (2004).
- [45] D. A. Hutcheon, S. Bishop, L. Buchmann, M. L. Chatterjee, A. A. Chen, J. M. D'Auria, S. Engel, D. Gigliotti, U. Greife, D. Hunter, et al., Nucl. Instr. Meth. **A 498**, 190 (2003).
- [46] R. O. Sayer, Rev. de Phys. App. **12**, 1543 (1977).
- [47] D. Gigliotti, Ph.D. thesis, Univ. of Northern British Columbia (2004).
- [48] J. A. Cameron and B. Singh, Nucl. Data Sheets **88**, 299 (1999).
- [49] J. F. Ziegler, J. P. Biersack, and U. Littmark, *The Stopping and Range of Ions in Solids* (Pergamon Press, New York, 1985).
- [50] J. F. Ziegler, *The stopping and range of ions in solids*, <http://srim.org> (2007).
- [51] W. A. Fowler, G. R. Caughlan, and B. A. Zimmerman, Annu. Rev. Astron. Astrophys. **5**, 525 (1967).
- [52] W. J. Thompson and C. Iliadis, Nuclear Physics A **647**, 259 (1999).
- [53] W. Hauser and H. Feshbach, Phys. Rev. **87**, 366 (1952).
- [54] M. Arnould and S. Goriely, Nucl. Phys. A **777**, 157 (2006).
- [55] U. Strohmusch, C. L. Fink, B. Zeidman, R. G. Markham, H. W. Fulbright, and R. N. Horoshko, Phys. Rev. **C 9**, 965 (1974).
- [56] H. W. Fulbright, C. L. Bennett, R. A. Lindgren, R. G. Markham, S. C. McGuire, G. C. Morrison, U. Strohmusch, and J. Töke, Nucl. Phys. A **284**, 329 (1977).
- [57] D. Frekers, H. Eickhoff, H. Löhner, K. Poppensieker, R. Santo, and C. Wiezorek, Z. Phys. A **276**, 317 (1976).
- [58] D. Frekers, R. Santo, and K. Langanke, Nucl. Phys. A **394**, 189 (1983).
- [59] F.-K. Thielemann, J. W. Truran, and M. Arnould, in *Advances in Nuclear Astrophysics*, edited by E. Vangioni-Flam, J. Audouze, M. Casse, J.-P. Chieze, and J. Tran Thanh van (1986), pp. 525–540.
- [60] Instead of the rate given in Ref. [25] as a fitted function we use the original reaction rate table [26] because the fitted function shows a different behavior and results in a lower  $^{44}\text{Ti}$  yield in the simulation of the  $\alpha$ -rich freeze-out; compare NON-SMOKER rate in Table IV and standard rate in Table V.